Materials Horizons

ROYAL SOCIETY OF CHEMISTRY

COMMUNICATION

View Article Online
View Journal | View Issue

Cite this: *Mater. Horiz.*, 2023, 10, 2109

Received 1st January 2023,
Accepted 6th March 2023

DOI: 10.1039/d3mh00001j

rsc.li/materials-horizons

Dual-infinite coordination polymer-engineered nanomedicines for dual-ion interference-mediated oxidative stress-dependent tumor suppression†

Junlie Yao,[ab] Jie Xing,[a] Fang Zheng,[a] Zihou Li,[a] Shunxiang Li,[a] Xiawei Xu,[a] Devrim Unay,[d] Young Min Song,[e] Fang Yang *[ac] and Aiguo Wu *[ac]

Recently, nanomedicine design has shifted from simple nanocarriers to nanodrugs with intrinsic antineoplastic activities for therapeutic performance optimization. In this regard, degradable nanomedicines containing functional inorganic ions have blazed a highly efficient and relatively safe ion interference paradigm for cancer theranostics. Herein, given the potential superiorities of infinite coordination polymers (ICPs) in degradation peculiarity and functional integration, a state-of-the-art dual-ICP-engineered nanomedicine is elaborately fabricated *via* integrating ferrocene (Fc) ICPs and calcium–tannic acid (Ca–TA) ICPs. Thereinto, Fc ICPs, and Ca–TA ICPs respectively serve as suppliers of ferrous iron ions (Fe^{2+}) and calcium ions (Ca^{2+}). After the acid-responsive degradation of ICPs, released TA from Ca–TA ICPs facilitated the conversion of released ferric iron (Fe^{3+}) from Fc ICPs into highly active Fe^{2+}. Owing to the dual-path oxidative stress and neighboring effect mediated by Fe^{2+} and Ca^{2+}, such a dual-ICP-engineered nanomedicine effectively induces dual-ion interference against triple-negative breast cancer (TNBC). Therefore, this work provides a novel antineoplastic attempt to establish ICP-engineered nanomedicines and implement ion interference-mediated synergistic therapy.

New concepts

As a promising oncotherapy paradigm with low invasiveness and high controllability, the exploitation of nanoprodrugs is still in its infancy. This work proposes the concept of two-or-more-infinite coordination polymer (ICP)-engineered nanomedicines and confirms their feasibility as a nanoprodrug. Concretely, acid-responsive degradable Fc@Ca–TA nanosystems have been fabricated in a novel way without following cumbersome synthetic procedures using integrating ferrocene (Fc) derivative-ferric iron (Fe^{3+}) ICPs and tannic acid (TA)–calcium (Ca^{2+}) ICPs. Thereinto, Ca–TA ICPs, which have never been reported in the nanotechnology and medicine fields, realize the improvement of Ca^{2+} overload nanoplatforms, since previously reported nanoplatforms were mainly $CaCO_3$, CaO_2, or CaP-based nanomaterials. Furthermore, dual-ion interference (a cutting-edge antitumor strategy) based on Fc@Ca–TA nanomedicines, namely ferrous iron ion (Fe^{2+}) based reactive oxygen species (ROS) generation and Ca^{2+} based overload effect, can significantly realize synergistically induced oxidative stress against triple-negative breast cancer (TNBC). In addition, the neighboring effect based on ion interference has been innovatively proposed and initially verified. As the first report about two-or-more-ICP-engineered nanomedicines for multi-ion interference, this work holds great potential for the establishment of nanoprodrugs and the advancement of synergistic tumor therapy.

Introduction

Recent decades have witnessed the blooming of nanomedicines and realize a paradigm shift in oncotherapy and secure their places as "magic bullets" driven by the breakthrough of nanomaterials.[1] Significantly distinguished from the first-generation nanomedicines dedicated to the morphological and structural regulation for efficient drug payload, the latest-generation nanomedicines have transferred their functionality from nanocarriers to nanodrugs featuring intrinsic antineoplastic activities.[2–4] Impressively, this trend has brought about numerous superiorities, such as optimized therapeutic efficiency (integrating antitumor effects and nano-level pharmacokinetics), simplified synthesis procedure (omitting drug encapsulation) as well as biosecurity management (no longer administering the toxicity and immunogenicity profiles of

[a] *Cixi Institute of Biomedical Engineering, International Cooperation Base of Biomedical Materials Technology and Application, Chinese Academy of Sciences (CAS) Key Laboratory of Magnetic Materials and Devices, Zhejiang Engineering Research Center for Biomedical Materials, Ningbo Institute of Materials Technology and Engineering, CAS, Ningbo 315201, China. E-mail: yangf@nimte.ac.cn, aiguo@nimte.ac.cn*
[b] *University of Chinese Academy of Sciences, No. 1 Yanqihu East Road, Huairou District, Beijing, 101408, China*
[c] *Advanced Energy Science and Technology Guangdong Laboratory, Huizhou 516000, China*
[d] *Electrical and Electronic Engineering Izmir Democracy University, Karabaglar 35140, Turkey*
[e] *School of Electrical Engineering and Computer Science, Gwangju Institute of Science and Technology, Gwangju 61005, Republic of Korea*

† Electronic supplementary information (ESI) available. See DOI: https://doi.org/10.1039/d3mh00001j

nanocarriers and drugs separately).[5] Nevertheless, the adverse effects of such nanomedicines remain a stumbling block, since they generally offer high natural toxicity to achieve potent antitumor efficacy. Nanoprodrugs, a promising concept to solve the aforementioned dilemma, are extremely low-toxic drug precursors meeting the requirements to become active therapeutic agents in the target region through chemical conversion.[6] In this sense, the exploitation of nanoprodrugs based on revolutionized nanomaterial combination and design is expected to blaze a new path for the next-generation nanomedicines, yet a fairly slow, challenging, and demanding process.

As an essential property of nanomedicines in biological applications, biodegradability is tremendously arousing great interest and offering significant inspiration recently.[7] Depending on the chemical composition, the degradation of nanomedicines can generate a mass of organic molecules and inorganic ions, which used to be regarded as waste components and smoothly discharged from the body.[8] Nowadays, ion interference has been a central antitumor topic overturning the traditional thinking mode, which is implicated in the aberrant distribution of ions in cancer cells and the resulting dysfunction of biological processes (*e.g.*, irreversible physical damage, cytotoxic ingredient generation, and apoptosis induction).[9,10] For instance, calcium (Ca^{2+}) overload is eligible to induce severe oxidative stress, which involves reactive oxygen species (ROS) generation, mitochondrial morphology change, and mitochondrial respiration disturbance.[11] Meanwhile, ferrous iron (Fe^{2+}) can catalyze the hydrogen peroxide (H_2O_2) overexpressed in tumor mitochondria through a localized Fenton reaction, thus yielding highly active hydroxyl radical ($^{\bullet}OH$) to trigger mitochondrial dysfunction.[12] Conceivably, the variety and quantity of therapeutic ions for ion interference can be predesigned in the fabrication of nanoparticles (NPs) and generated as required during degradation. In parallel, with the introduction of the tumor microenvironment (TME) responsive concept, therapeutic ions that are initially confined in degradable nanosystems and eventually released in the TME can be relatively low off-target toxic, hence exhibiting sufficient potential as a promising prodrug.

Deemed as a type of cutting-edge degradable nanosystems, infinite coordination polymers (ICPs) are amorphous compounds harnessing coordination bonds to connect ligands and metal ions directly.[13] For instance, burgeoning metal–phenolic ICPs are formed by the coordination between phenolic ligands and metal ions, which therefore inherit the biological activity of polyphenols and the imaging/therapeutic properties of metal ions.[14] As the coordination bonds within ICPs are extremely sensitive to acid, ICPs realize biosafety and biodegradability, *i.e.*, not disintegrating until reaching the acidic tumor tissue.[15] Currently, ICPs have been a welcome addition to the nanoprodrugs available for oncotherapy, owing to their high agent payload, perfect therapeutic performance, minimal side effects, extended functionality, and so forth.[16] Nevertheless, the investigations in this direction are still in their infancy due to the need for multidisciplinary integration (*e.g.*, material, chemical, pharmaceutical, biological, and medical sciences). In particular, there is a lack of two-or-more-ICP-engineered nanomedicines providing remarkable super-additive therapeutic effects for synergistic antineoplastic strategies.

Despite the progress in various nanomedicines, triple-negative breast cancer (TNBC) still remains a huge threat to society due to the resistance mechanism, which urgently waits for more in-depth explorations of innovative therapeutic options.[17] Herein, with the prospects of highlighting the underlying superiorities of ICP-engineered nanomedicines, two types of ICPs based on ferrocene (Fc) derivative/ferric iron (Fe^{3+}) and tannic acid (TA)/Ca^{2+} respectively, were integrated into a novel nanosystem (Fc@Ca–TA NPs) as a nanoprodrug model against TNBC. In this nanosystem, the interior Fc ICPs served as a Fe^{2+} supplier to generate $^{\bullet}OH$ and destroy oxidation equilibrium, thereby existing as an effective form of mitochondrial destruction.[18] Withal, owing to the pH-dependent degradation characteristic of Fc@Ca–TA NPs, unconfined Fe^{2+}/Fe^{3+} from Fc ICPs imparted TME-responsive magnetic resonance (MR) imaging for the visualization of the tumor area.[19] Furthermore, during the degradation process, the exterior Ca–TA ICPs were eligible to release both TA and Ca^{2+}. Thereinto, the TA was able to convert Fe^{3+} released from Fc ICPs into high catalytic-active Fe^{2+}, thus replenishing the Fe^{2+} supply for Fc ICPs to induce more efficient oxidative stress.[20] In addition, the up-regulation of Ca^{2+} was especially beneficial to disturb mitochondrial function, which collaborated with Fe^{2+} interference to overturn oxidation homeostasis.[21] When two functional ions induce cell apoptosis, liberated ions from dead or dying cells can further infect surrounding cells, thus amplifying their therapeutic effects through the neighboring effect.[22] By taking full advantage of the aforementioned synergistic mechanisms, tumor proliferation can be availably restrained by the cell death regulation of Fc@Ca–TA NPs. In summary, this work enlightens the design and exploitation of ICP-engineered nanomedicines and proposes a cutting-edge orientation for future ion interference-mediated synergistic therapy.

Results and discussion

Preparation and characterization of Fc@Ca–TA NPs

In brief, the preparation technique of Fc@Ca–TA NPs was divided into two steps: the synthesis of Fc NPs and the introduction of Ca–TA (Fig. S1, ESI†). First, Fc ICPs were prepared by referencing a previous method,[23] which involved the light-triggered Fe^{2+} release and 1,1′-ferrocenedicarboxylic acid deprotonation, the oxidation of free Fe^{2+} into Fe^{3+}, and the coordination of Fe^{3+} and deprotonated 1,1′-ferrocenedicarboxylic acid. Importantly, LED light with power as low as 0.02 W (a daily table lamp) was adapted as an exogenous energy source for photodegradation instead of previously reported natural light and xenon light to make the preparation more flexible in time and cast off expensive equipment to some extent. After the cladding of DSPE-PEG on the surface of Fc ICPs, spherical ICPs NPs were synthesized, as shown in Fig. 1a and Fig. S2 (ESI†). In addition to improving the hydrophilicity,

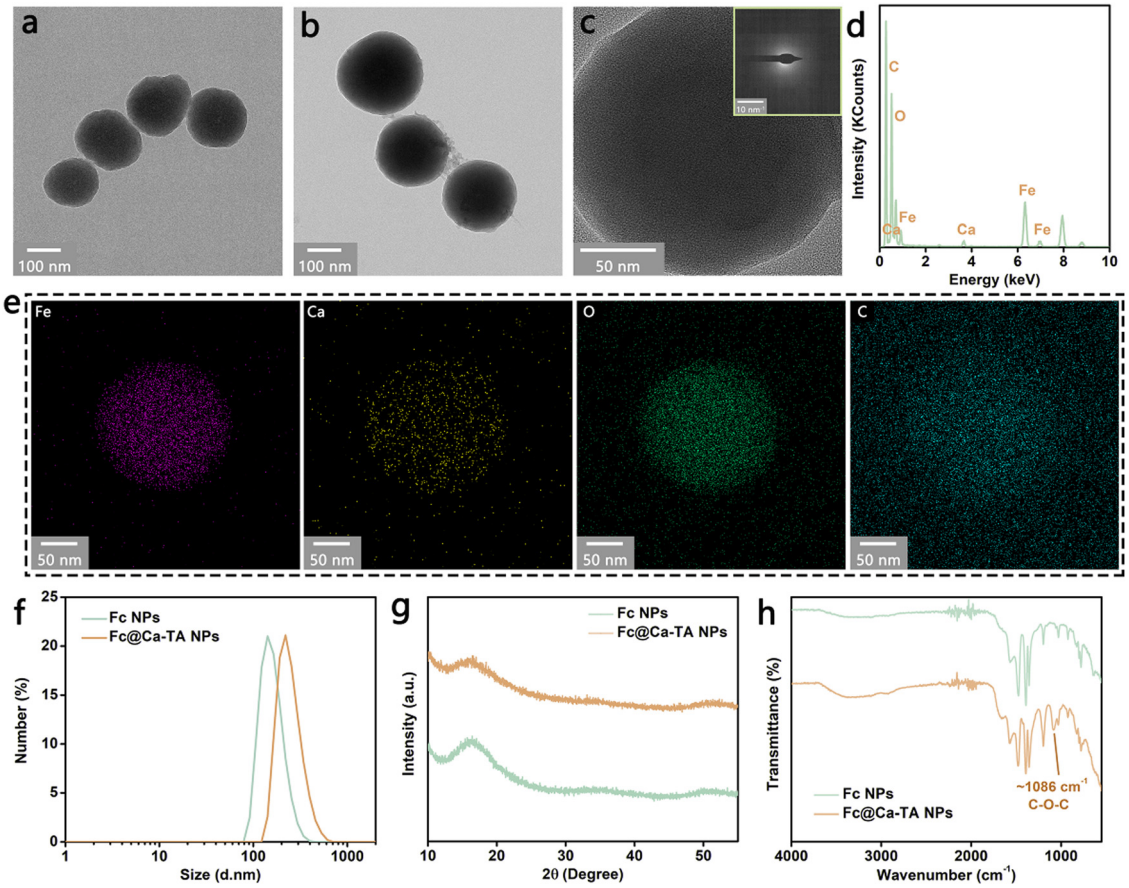

Fig. 1 Preparation and characterization of Fc@Ca–TA NPs. (a and b) TEM images of Fc NPs and Fc@Ca–TA NPs. (c) High-magnification TEM image and SAED pattern of Fc@Ca–TA NPs. (d) EDS spectrum of Fc@Ca–TA NPs. (e) Elemental mapping of Fc@Ca–TA NPs. (f) DLS curves of Fc NPs and Fc@Ca–TA NPs. (g) XRD patterns of Fc NPs and Fc@Ca–TA NPs. (h) FT-IR spectrum of Fc NPs and Fc@Ca–TA NPs.

DSPE-PEG effectively protected the spherical frame of Fc ICPs from coordination competition in the subsequent Ca–TA coordination process (Fig. S3, ESI†). Second, Ca–TA ICPs, to our knowledge, firstly proposed in the nanotechnology and medicine fields, were manufactured on the surface of Fc NPs through the surface adsorption of free TA/small TA complexes to DSPE-PEG and subsequent coordination of Ca^{2+} and digalloyl groups in polyphenol TA (Fig. S4, ESI†).[24] This strategy of growing ICPs on liposomes holds promise for further utilization in a variety of engineered cells and bacteria as well as membrane mimetic biomaterials. Due to the hydrogen-bond interaction between TA and PVP, highly biocompatible PVP is well-suited for further encapsulation to obtain dual-ICP-engineered Fc@Ca–TA NPs, as shown in Fig. 1b and Fig. S5, S6 (ESI†).[25,26]

Since the principal components were amorphous ICPs, the obtained Fc@Ca–TA NPs were featured with an obvious amorphous state, without distinct lattice fringe in the transmission electron microscopy (TEM) analysis and diffraction characteristic in the selected area electron diffraction (SAED) analysis (Fig. 1c). Withal, the energy-dispersive X-ray spectroscopy (EDS) and elemental mapping analyses verified the efficient introduction of Ca^{2+} into Fc@Ca–TA NPs (Fig. 1d and e), compared with Fc NPs in the previous step (Fig. S7, ESI†). Besides, the dynamic light scattering (DLS) analysis illustrated that the average sizes of Fc NPs and Fc@Ca–TA NPs (containing hydration layers) were, respectively, 186.3 nm and 249.7 nm (Fig. 1f). Simultaneously, the polydispersity index of Fc@Ca–TA NPs was 0.12, which embodied a suitable size distribution for biological applications. With regard to the crystal structures, typical widening peaks rather than diffraction peaks in the powder X-ray diffraction (XRD) analysis further proved the amorphous structure of Fc NPs and Fc@Ca–TA NPs (Fig. 1g). Besides, the X-ray photoelectron spectroscopy (XPS) analysis further illustrated the existence of Ca and Fe composition in the Fc@Ca–TA NPs (Fig. S8, S9, and S10, ESI†). Inductively coupled plasma optical emission spectrometry (ICP–OES) also indicated that the content ratio of Fe to Ca in the Fc@Ca–TA NPs was 72.7% : 27.3% (Fig. S11, ESI†). In parallel, there were no significant absorption peaks in the ultraviolet-visible (UV-vis) spectra of Fc NPs and Fc@Ca–TA NPs (Fig. S12, ESI†). Furthermore, Fourier transform infrared (FT-IR) and zeta potential analyses were engaged for the superficial property detections. As shown in Fig. 1h, the bands appeared at 1086 cm^{-1} referred to the C–O–C of TA, which could adequately certify the effective integration of Fc NPs and Ca–TA ICPs by combining with the

previously confirmed presence of Ca^{2+}. Additionally, both water-dispersible Fc NPs and Fc@Ca–TA NPs were negatively charged with electricity (Fig. S13, ESI†). In a word, the aforementioned results demonstrated the successful prescription and preparation of dual-ICP-engineered Fc@Ca–TA NPs.

Theranostic performance of Fc@Ca–TA NPs

Above all, the degradation properties of Fc@Ca–TA NPs were comprehensively evaluated to explore the development potential as a degradable nanoprodrug. Intuitively, the structure of Fc@Ca–TA NPs decomposed over time in a slightly acidic environment at pH 5.5 (Fig. 2a and Fig. S14, ESI†). As a supplementary, proton-triggered Fe and Ca release after Fc@Ca–TA NPs degradation were investigated, and their release amounts at 24 h were 44.6% and 73.2%, respectively, thus revealing the pH-responsive dual-ion provision of Fc@Ca–TA NPs (Fig. 2b and c). Meanwhile, Ca–TA ICPs on the outside were preferentially in contact with the proton compared to the Fc ICPs on the inside of the DSPE-PEG layer, thus showing a higher ion release efficiency. In addition, MR imaging performance based on the Fe release was traced to determine the feasibility of providing tumor lesion information in real time. Obviously, T_1-weighted MR contrast enhancement was positively correlated with Fe concentration at pH 5.5, accompanied by a longitudinal relaxivity (r_1) value up to 7.502 mM^{-1} s^{-1}, while no significant change in the signal intensity arose at pH 7.4 (Fig. 2d and Fig. S15, S16, ESI†). From another aspect, the catalytic properties of Fc@Ca–TA NPs as a Fenton agent were methodically investigated. In the 1,10-phenanthroline colorimetric assay for Fe^{2+} detection, the generated orange ferrous complexes at pH 5.5, with the characteristic absorption peak at 510 nm, strongly supported the existence of free Fe^{2+}, which may be ascribed to the direct supply pathway of 1,1′-ferrocenedicarboxylic acid as well as the indirect supply pathway of Fe^{3+} and TA (Fig. 2e). Analogously, in the TMB assay for •OH detection, the characteristic absorption peak of oxidized TMB at 652 nm signifying the •OH generation only appeared at pH 5.5, due to the structure integrality of Fc@Ca–TA NPs at pH 7.4 and the resulting absence of free Fe^{2+} (Fig. 2f and Fig. S17, ESI†). In good accordance with the TMB assay, there was a strong •OH signal at pH 5.5 by using ESR as a more intuitive measurement. In a nutshell, Fc@Ca–TA NPs had

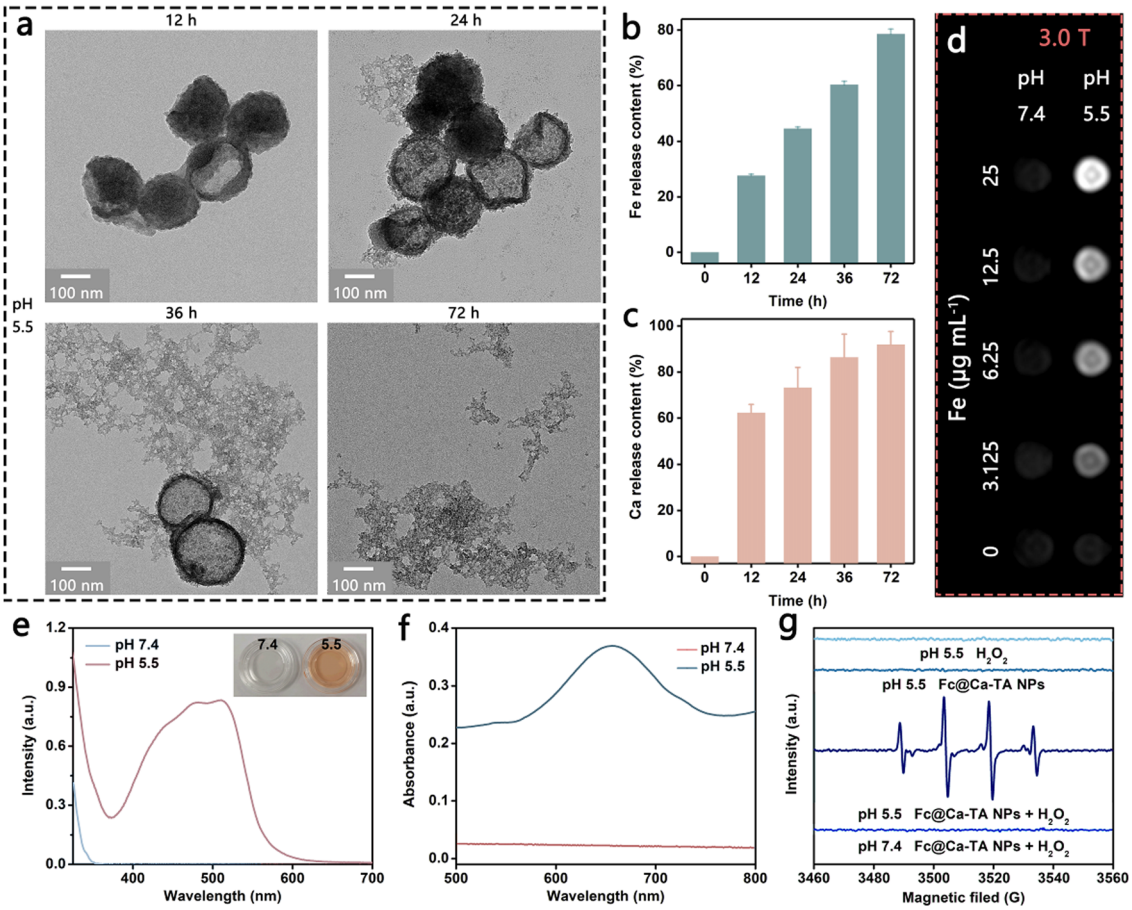

Fig. 2 Theranostic performance of Fc@Ca–TA NPs. (a) TEM images of Fc@Ca–TA NPs treated with a mild acid. (b and c) Fe release and Ca release from Fc@Ca–TA NPs treated with a mild acid. (d) T_1-weighted MR images of Fc@Ca–TA NPs treated with different pH conditions. (e) Colorimetry of 1,10-Phenanthroline treated with different pH conditions (Fe in Fc@Ca–TA NPs: 50 μg mL^{-1}). (f) Oxidation of TMB treated with different pH conditions (Fe in Fc@Ca–TA NPs: 10 μg mL^{-1}, H_2O_2:1 mM). (g) •OH measurement *via* ESR spectra (Fe in Fc@Ca–TA NPs: 10 μg mL^{-1}, H_2O_2:1 mM). Data are presented as the mean ± SD (n = 3).

the potential to serve as a degradable nanoprodrug, offering a dramatic opportunity to integrate dual-ion interference and pH-responsive MR imaging.

Synergistic effect of calcium and iron

Ca^{2+} overload and intracellular free radicals are promising to mediate a synergistic antineoplastic effect due to their mutual causation.[11] In this regard, Fe^{2+} holds great promise in •OH up-regulation, thus showing an inextricable link to calcium homeostasis. Based on this, we infer that Ca^{2+} and Fe^{2+} could induce a synergistic antitumor effect and conduct related investigations (Fig. 3a). For starters, there is a total of 66 overlapping genes among calcium and iron homeostasis-related genes from MSigDB online database (https://www.gsea-msigdb.org/gsea/login.jsp), showing a significant intersection between calcium and iron homeostasis (Fig. 3b). In order to explore the combination therapeutic potential of Ca^{2+} and Fe^{2+}, the death situation of TNBC breast cancer cells (MDA-MB-231) incubated with dual ions was explored (Fig. 3c). Compared with single ion interference, combination interference achieved a more efficient inhibition effect at a lower dosage, availably demonstrating the effectiveness and safety of combination strategy. Additionally, Fe^{2+} ions were capable even to up-regulate the intracellular level of Ca^{2+} ions indirectly, which demonstrated the close association between calcium and iron homeostasis (Fig. 3d). Furthermore, the MDA-MB-231 line was selected to compare the antitumor effects of Fc NPs (Fe^{2+} supply) with Fc@Ca–TA NPs (Ca^{2+} and Fe^{2+} dual-supply). As expected, the survival rate of MDA-MB-231 cells treated

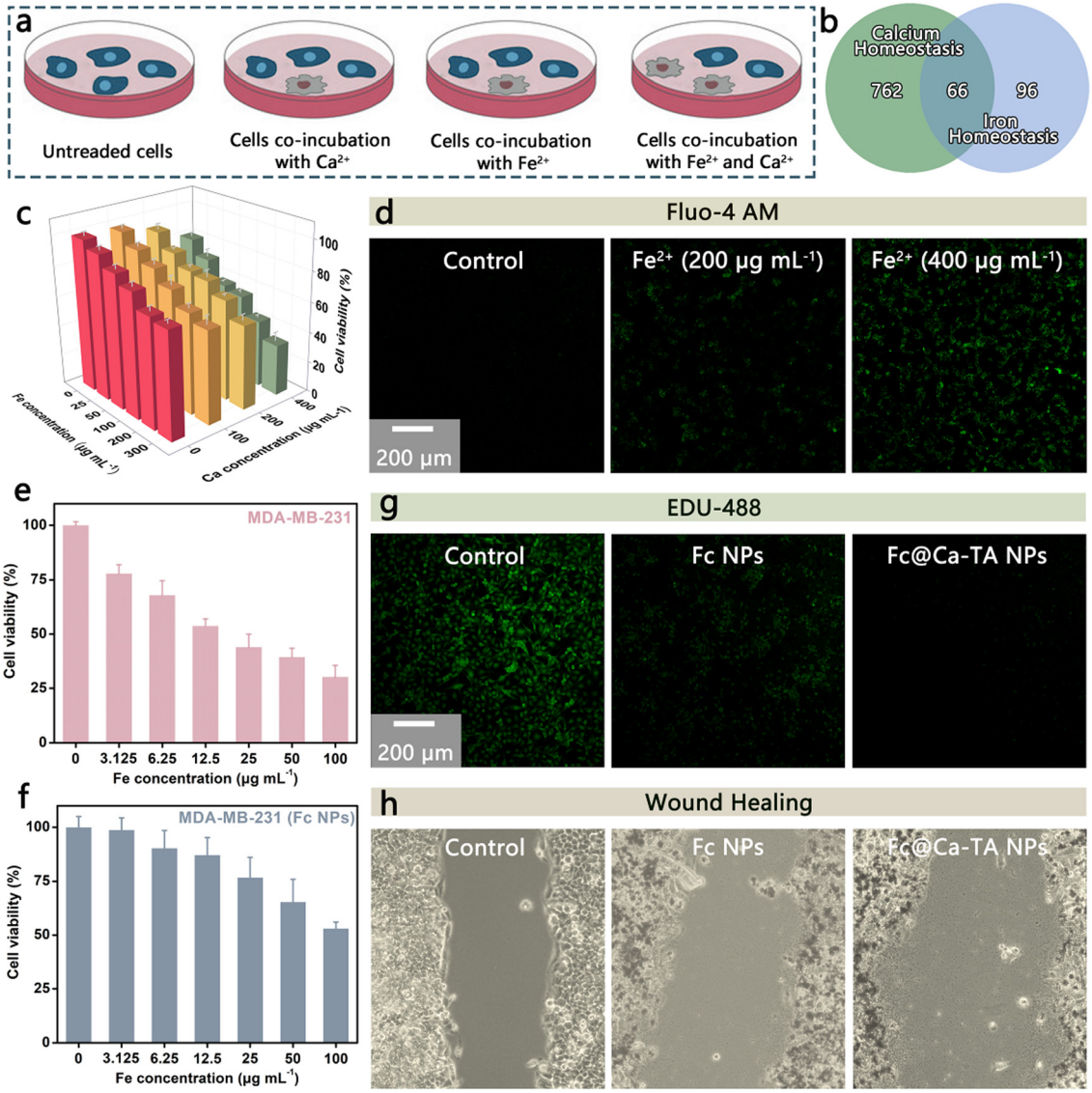

Fig. 3 Synergistic effect of calcium and iron. (a) Schematic illustration of the cell survival incubated with different ions. (b) Overlapping genes among the calcium and iron homeostasis groups. (c) Cell viability of MDA-MB-231 cells incubated with Ca^{2+} and Fe^{2+} for 24 h. (d) Fluorescence images of MDA-MB-231 cells stained with Fluo-4 AM. (e) Cell viability of MDA-MB-231 cells incubated with Fc@Ca–TA NPs for 24 h. (f) Cell viability of MDA-MB-231 cells incubated with Fc NPs for 24 h. (g) Fluorescence images of MDA-MB-231 cells stained with EDU 488 (Fe in Fc@Ca–TA NPs and Fc NPs: 100 μg mL^{-1}). (h) Microscopy images of scratch experiments (Fe in Fc@Ca–TA NPs and Fc NPs: 100 μg mL^{-1}). Data are presented as the mean ± SD (n = 5).

with Fc@Ca–TA NPs was lower than those treated with Fc NPs (Fig. 3e and f). In addition to more efficiently inhibiting cell proliferation, Fc@Ca–TA NPs had a more obvious influence on cell metastasis than Fc NPs, embodying that calcium overload induced by direct Ca^{2+} up-regulation could effectively cooperate with iron interference (Fig. 3g and h). Therefore, the aberrant distribution of Ca^{2+} and Fe^{2+} ions mediated by Fc@Ca–TA NPs is a promising way to induce a synergistic intervention effect efficiently interfering with the functional homeostasis of cancer cells.

Biosafety of Fc@Ca–TA NPs

Systematic experiments at the cellular and animal levels were further executed to evaluate the biological potential of Fc@Ca–TA NPs. Initially, the normal fibroblast cell line (3T3), MDA-MB-231 line, and estrogen receptor (ER)-positive breast cancer cell line (MCF-7) were selected for the biocompatibility and cytotoxicity of Fc@Ca–TA NPs by the CCK-8 assay. The survival rate of 3T3 cells incubated with diverse concentrations of Fc@Ca–TA NPs degraded slightly. It still remained at 84.5% even though the Fe concentration was high (100 μg mL^{-1}), demonstrating the safety of Fc@Ca–TA NPs in normal cells (Fig. 4a). Nevertheless, both MDA-MB-231 and MCF-7 cells incubated with Fc@Ca–TA NPs exhibited significant concentration-dependent mortality (Fig. 3e and Fig. S18, ESI†). Specifically, as the Fe concentration of Fc@Ca–TA reached 100 μg mL^{-1}, the survival rate of MDA-MB-231 cells declined to 30.2%. To explain this phenomenon, the intracellular pH difference between 3T3 and MDA-MB-231 cells was explored *via* the fluorescence probe BCECF AM. There was a higher fluorescence intensity (*i.e.*, higher pH value) in 3T3 cells, which was adverse to the degradation of Fc@Ca–TA and subsequent ion interference. Meanwhile, normal cells exhibited much lower uptake than tumor cells, which was another reason for their high tolerance (Fig. S19, ESI†). In parallel, significantly reduced cell colonies in the crystal violet staining assay also indicated the satisfactory inhibitory effect of Fc@Ca–TA NPs on MDA-MB-231 cell proliferation (Fig. S20, ESI†). As for the cellular uptake behavior of Fc@Ca–TA NPs, the bio-TEM image confirmed the efficient ingestion of MDA-MB-231 cells to Fc@Ca–TA NPs (Fig. 4c). Furthermore, the blood biochemistry and hematology assays, as an indispensable step before clinical application, were conducted to further notarize the suitability of Fc@Ca–TA NPs. By comparison, various indexes of BALB/c mice receiving

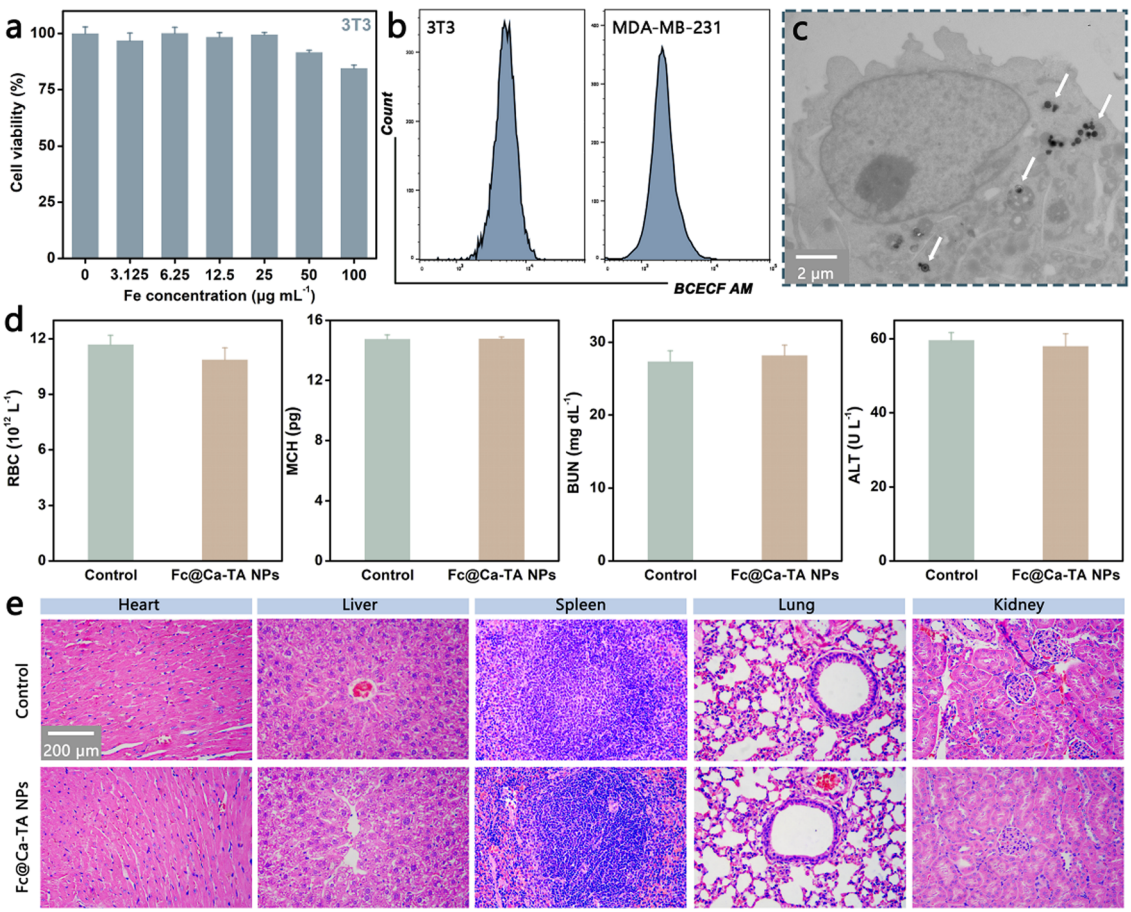

Fig. 4 Biosafety of Fc@Ca–TA NPs. (a) Cell viability of 3T3 cells incubated with Fc@Ca–TA NPs for 24 h. (b) Intracellular pH analysis of 3T3 cells and MDA-MB-231 cells. (c) Bio-TEM image of MDA-MB-231 cells incubated with Fc@Ca–TA NPs (Fe in Fc@Ca–TA NPs: 100 μg mL^{-1}) for 6 h. (d and e) Blood biochemistry, hematology and H&E staining images of mice intravenously injected with Fc@Ca–TA NPs (Fe: 8 mg mL^{-1}, 100 μL) or saline. Data are presented as the mean ± SD (n = 5).

intravenous injections of Fc@Ca–TA NPs were maintained within a normal range (Fig. 4d and Fig. S21, ESI†). In addition, no pathological damage appeared in the major organs of the experimental mice receiving intravenous injection of Fc@Ca–TA NPs (Fig. 4e). In short, the above-mentioned results convincingly illustrated that Fc@Ca–TA NPs at the right concentration were distinguished with engaging biosafety as a promising antitumor nanoprodrug.

Antitumor mechanisms of Fc@Ca–TA NPs

Inspired by the theranostic properties of Fc@Ca–TA NPs, their specific antitumor mechanisms were further explored using the MDA-MB-231 cell line. According to the pH-responsive degradation characteristic of Fc@Ca–TA NPs, the generation of Fe^{2+} and Ca^{2+} inside MDA-MB-231 cells was respectively monitored by potassium ferricyanide staining and alizarin red staining. As shown in Fig. 5a and Fig. S22 (ESI†), conspicuously amplified blue and red areas implied the formation of metal complexes after co-incubation with Fc@Ca–TA NPs, which provided potent evidence of the produced Fe^{2+} and Ca^{2+}. Besides, Fluo-4 AM (a Ca^{2+} fluorescent probe) was applied to complementarily illustrate the occurrence of Ca^{2+} overload. Analogously, significantly elevated green fluorescence appeared after co-incubation with Fc@Ca–TA NPs (Fig. 5b). Thereafter, the synergistically induced oxidative stress based on Fe^{2+} and Ca^{2+} was systematically investigated. First of all, vitamin C (VC) and vitamin E (VE) are regarded as natural antioxidants to alleviate oxidative stress, contributing to improving the survival of MDA-MB-231 cells treated by Fc@Ca–TA NPs, which suggests that the oxidation balance disruption is an important cause of cell death (Fig. 5c and d). Meanwhile, there was an obvious volume reduction of mitochondria and extensive vacuolization of the endoplasmic reticulum in the treated MDA-MB-231 cells, implying effective oxidative stress and organelle damage (Fig. 5e).[27] Ulteriorly, intracellular ROS generation, and mitochondrial membrane potential were directly measured using DCFH-DA, JC-1, and Rho 123 fluorescent probes, certifying the noticeable ROS up-regulation as well as mitochondrial dysfunction induced by Fc@Ca–TA NPs (Fig. 5f). Accompanied by the mitochondrial dysfunction, the intracellular ATP level was significantly decreased (Fig. S23, ESI†). Moreover, intracellular GSH and SOD (two types of natural intracellular antioxidants) levels were down-regulated visibly by Fc@Ca–TA NPs, indirectly displaying the destruction of Fc@Ca–TA NPs to the oxidation defense system of MDA-MB-231 cells (Fig. 5g).[28,29] To further explore the cell death mode, the antitumor efficiency of Fc@Ca–TA NPs was investigated through the annexin V-FITC/PI assay. Unlike normal MDA-MB-231 cells, those incubated with Fc@Ca–TA NPs were seriously impaired due to apoptosis induction. To be specific, the apoptosis rate of MDA-MB-231 cells increased to 84.3% when the Fe concentration was 100 μg mL^{-1} (Fig. 5h). Furthermore, common apoptosis factors, namely, Caspase-3, Caspase-8, and Caspase-9 were effectively up-regulated (Fig. S24, ESI†).[30] Based on the above analyses, Fc@Ca–TA NPs may induce an apoptosis cellular regulatory pathway and override the resistance mechanism of MDA-MB-231 cells to achieve cell death. Therefore, these results at the cellular level demonstrated that Fc@Ca–TA NPs effectively mediated dual-ion interference-based mitochondrial oxidative stress, thus relentlessly striking and eliminating MDA-MB-231 cells.

Neighboring effect of Fc@Ca–TA NPs

The neighboring effect means that tumor cells may have the potential to be converted into an *in situ* drug depot, once as-ingested drugs are superfluous and liberated from dead or dying cells after inducing cell apoptosis.[22] Based on this, we suppose that liberated ions could execute an effective neighboring effect after the tumor cell death for intercellular transport and continued apoptosis induction and conduct relevant investigations (Fig. 6a). As expected, there was significant membrane damage in the MDA-MB-231 cells after co-incubation with Fc@Ca–TA NPs, testified by markedly diminished fluorescence in DiR membrane staining (Fig. 6b). In addition, the release of cytoplasmic lactate dehydrogenase (LDH) was also valid as an argument for plasma membrane rupture (Fig. 6c). Besides, the cellular morphology of MDA-MB-231 cells after co-incubation with Fc@Ca–TA NPs was appraised by SEM (Fig. S25, ESI†). There was a marked rupture in MDA-MB 231 cells, thereby embodying the possibility of a large outflow of ions. Whereafter, fresh DMEM (Group Control-1), DMEM after 24 h co-incubation with MDA-MB-231 cells (Group Control-2), and DMEM after 24 h co-incubation with MDA-MB-231 cells and Fc@Ca–TA NPs (Group Fc@Ca–TA NPs) were collected for subsequent apoptosis induction. After staining with alizarin red, potassium ferricyanide, and 1,10-phenanthroline, respectively, the dark red color of DMEM in Group Fc@Ca–TA NPs implied the presence of large amounts of released Ca^{2+}, while the green and orange color of DMEM in Group Fc@Ca–TA NPs corresponded to the presence of Fe^{2+} (Fig. 6d, e and f). Meanwhile, the release amounts of co-existing Ca^{2+} and Fe^{2+} severally reached 54.2% and 33.3% (Fig. 6g). Moreover, DMEM in Group Fc@Ca–TA NPs was relatively acidic due to the leakage of intracellular acid substance after the plasma membrane damage (Fig. S26, ESI†). After incubation with the above three types of DMEM, only the MDA-MB-231 cells in Group Fc@Ca–TA NPs died obviously on account of dual-ion interference-mediated apoptosis induction effects (Fig. 6h and i). Consequently, Fc@Ca–TA possessed the potential to amplify its antitumor effect through the neighboring effect based on the dual ions.

Tumor inhibition of Fc@Ca–TA NPs

To investigate the tumor inhibition performance of Fc@Ca–TA NPs under clinically relevant conditions, the MDA-MB-231 tumor-bearing mice model was established and validated to monitor the treatment response (Fig. 7a). During the therapeutic process, the body weight of mice fluctuated mildly within the normal range, displaying that the adopted therapeutic schemes were safe with little adverse effects (Fig. 7b). With regard to therapeutic efficacy, conspicuous tumor elimination occurred after the injection of Fc@Ca–TA NPs either intravenously or intratumorally (Fig. 7c and d). In addition, pathological histology analysis was imparted to further

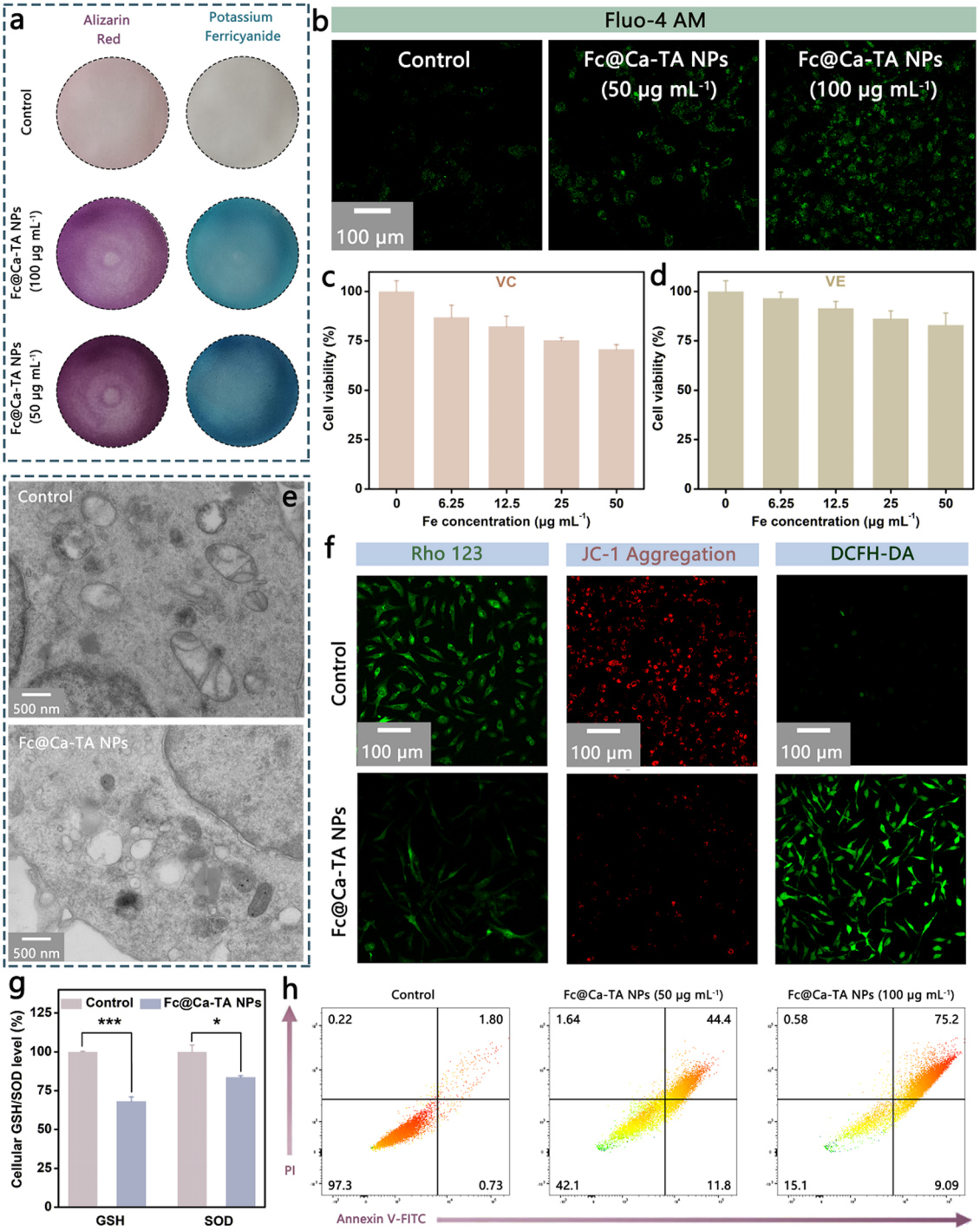

Fig. 5 Antitumor mechanisms of Fc@Ca–TA NPs. (a) Potassium ferricyanide staining and alizarin red staining of MDA-MB-231 cells incubated with Fc@Ca–TA NPs for 12 h. (b) Fluorescence images of MDA-MB-231 cells stained with Fluo-4 AM. (c and d) Cell viability of MDA-MB-231 cells incubated with Fc@Ca–TA NPs and VC (50 μM) or VE (200 μM). (e) Bio-TEM image of MDA-MB-231 cells incubated with Fc@Ca–TA NPs (Fe in Fc@Ca–TA NPs: 100 μg mL^{-1}) for 12 h. (f) Fluorescence images of MDA-MB-231 cells stained with DCFH-DA, JC-1, and Rho-123. (g) Intracellular GSH and SOD levels of MDA-MB-231 cells incubated with Fc@Ca–TA NPs (Fe in Fc@Ca–TA NPs: 100 μg mL^{-1}) for 12 h. (h) Apoptotic analysis of MDA-MB-231 cells incubated with Fc@Ca–TA NPs (Fe in Fc@Ca–TA NPs: 100 μg mL^{-1}) for 24 h. Data are presented as the mean ± SD (n = 5).

explore the pathological change in tumor tissue mediated by Fc@Ca–TA NPs (Fig. 7e and f). Specifically, H&E staining, TUNEL staining, and Ki67 staining affirmed the excellent tumor inhibition performance of Fc@Ca–TA NPs, demonstrated by obvious nucleus disappearance and membrane fragmentation. Meanwhile, there were noticeable calcified nodule and mitochondrial dysfunction characteristics, separately in the Von Kossa staining, alkaline phosphatase (ALP) staining, and

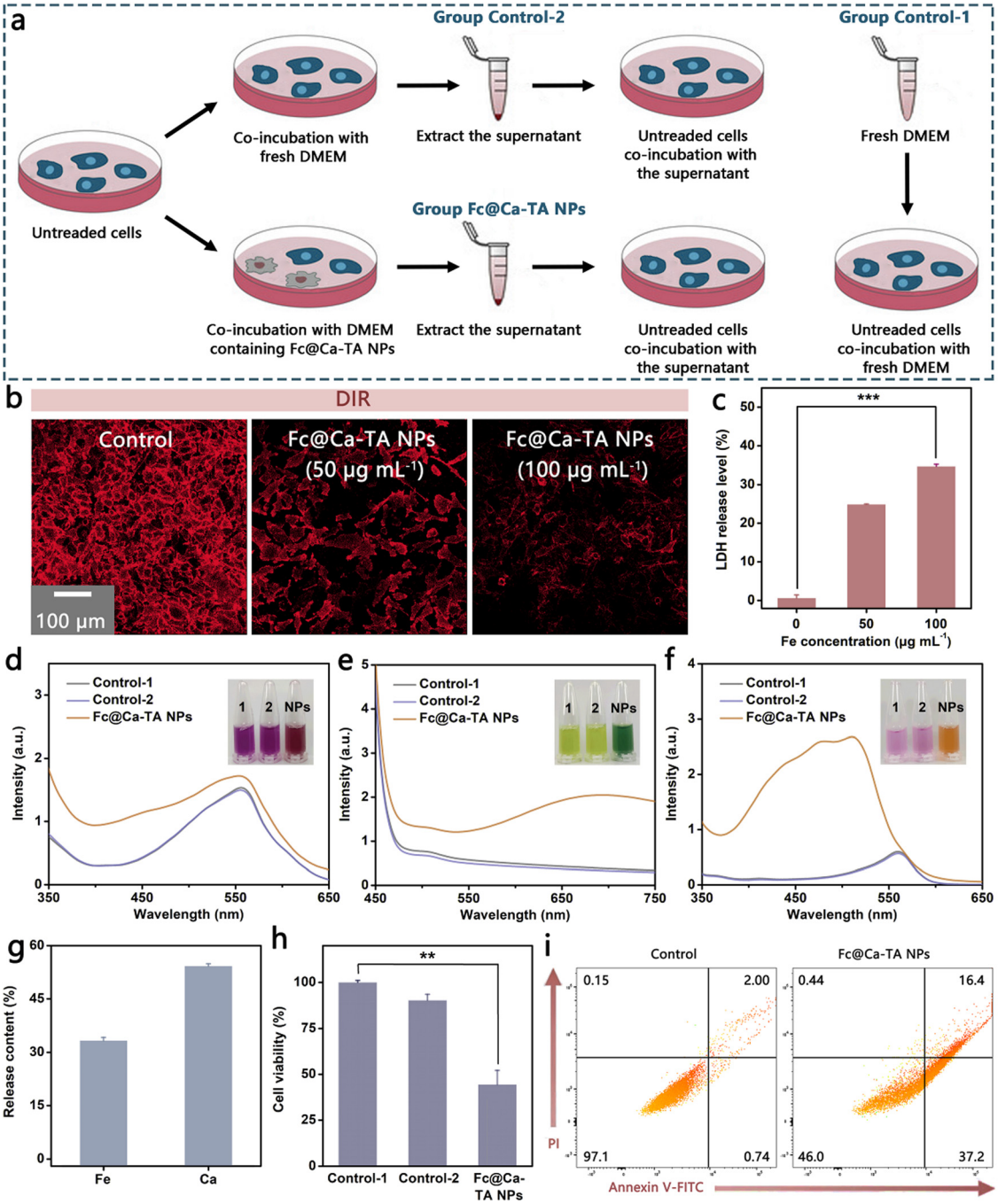

Fig. 6 Neighboring effect of Fc@Ca–TA NPs. (a) Schematic illustration of the experimental progress to verify the neighboring effect. (b) DiR staining of MDA-MB-231 cells incubated with Fc@Ca–TA NPs for 24 h. (c) Released LDH from MDA-MB-231 cells incubated with Fc@Ca–TA NPs for 24 h. (d–f) Colorimetry of alizarin red, potassium ferricyanide, and 1,10-Phenanthroline in the determination of Ca^{2+} and Fe^{2+}. (g) Free Fe^{2+} and Ca^{2+} in DMEM after different treatments. (h) Cell viability of MDA-MB-231 cells incubated with DMEM after treatments for 24 h. (i) Apoptotic analysis of MDA-MB-231 cells incubated with DMEM after different treatments for 24 h. [Group Control-1: fresh DMEM; Group Control-2: DMEM after 24 h co-incubation with MDA-MB-231 cells; Group Fc@Ca–TA NPs: DMEM after 24 h co-incubation with MDA-MB-231 cells and Fc@Ca–TA NPs (Fe in Fc@Ca–TA NPs: 100 μg mL^{-1})]. Data are presented as the mean ± SD (n = 5).

uncoupling protein 2 (UCP 2, a typical mitochondrial dysfunction indicator) staining assays.[31,32] Moreover, there was a clearly enhanced T_1 signal intensity within the tumor region at the post-intravenous or intratumoral injection of Fc@Ca–TA NPs, thereby demonstrating the pH-triggered imaging and therapeutic supervision abilities of Fc@Ca–TA NPs (Fig. 5f and Fig. S27, ESI†). As a consequence, as-prepared Fc@Ca–TA NPs ingeniously integrated therapeutic and imaging modalities, offering a reliable theranostic paradigm for MDA-MB-231 tumor Inhibition.

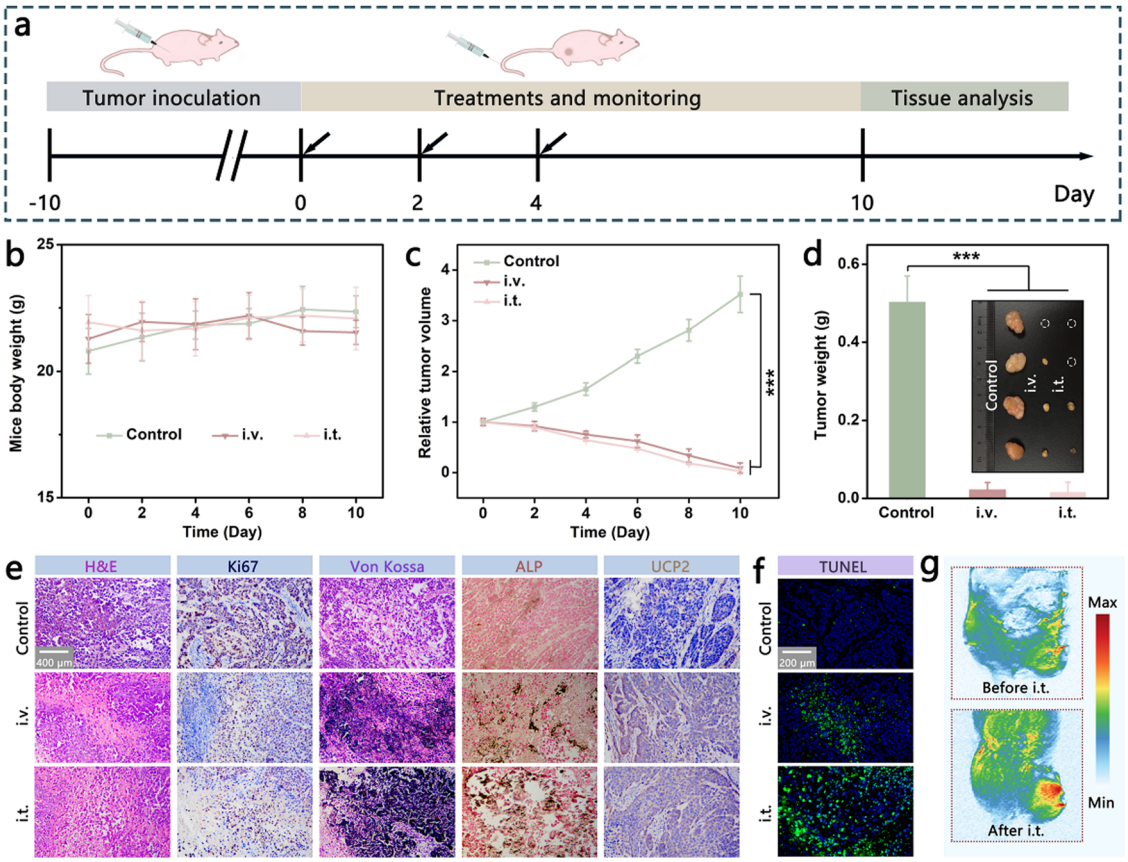

Fig. 7 Tumor inhibition of Fc@Ca–TA NPs. (a) Schedule of therapeutic process based on Fc@Ca–TA NPs. (b and c) Mice body weight and tumor volume curves after different treatments. (d) Tumor weights and tumor images at the treatment endpoint. (e) H&E, Ki67, Von Kossa, ALP, and UCP2 fluorescence-stained tumor sections after different treatments. (f) TUNEL fluorescence-stained tumor sections after different treatments. (g) MR images of mice intratumorally injected with Fc@Ca–TA NPs (Fe: 4 mg mL^{-1}, 50 μL). Data are presented as the mean ± SD (n = 4).

Conclusions

In summary, ICP-engineered Fc@Ca–TA NPs were fabricated *via* dexterously integrating Fc ICPs and Ca–TA ICPs, which served as "magic bullets" for highly efficient dual-ion-induced and MR imaging-guided mitochondrial oxidative stress against TNBC. Herein, the biosafety of Fc@Ca–TA NPs was demonstrated in detail, and their prominent therapeutic effects and mechanisms were comprehensively illustrated. On the one hand, this work is promising to enlighten the design and construction of nanomedicines in the near future, *e.g.*, functionalized ICPs, Ca^{2+} overload nanoplatforms, and MR imaging nanosystems. On the other, this work may provide a novel channel for applying multi-ion interference for oxidative stress-mediated tumor eradication.

Author contributions

Junlie Yao: methodology, investigation, formal analysis, data curation, writing – original draft. Jie Xing: investigation, conceptualization, writing – review, and editing. Fang Zheng: data curation, formal analysis. Zihou Li: formal analysis, validation. Sunxiang Li: methodology, validation. Xiawei Xu: methodology, validation. Devrim Unay: image analysis, visual images. Young Min Song: data curation, image analysis. Fang Yang: conceptualization, funding acquisition, supervision, writing – review, and editing. Aiguo Wu: funding acquisition, resources, project administration, supervision, writing – review, and editing.

Conflicts of interest

There are no conflicts to declare.

Acknowledgements

The authors are grateful for the financial support from the National Natural Science Foundation of China (32025021, 31971292, 32111540257), Youth Innovation Promotion Association, Chinese Academy of Sciences (2022301), and Ningbo 3315 Innovative Talent Project (2018-05-G).

Notes and references

1 J. Shi, P. W. Kantoff, R. Wooster and O. C. Farokhzad, *Nat. Rev. Cancer*, 2017, **17**, 20–37.
2 F. Tang, L. Li and D. Chen, *Adv. Mater.*, 2012, **24**, 1504–1534.

3 Y. Wang, J. Tang, Y. Yang, H. Song, J. Fu, Z. Gu and C. Yu, *Angew. Chem., Int. Ed.*, 2020, **59**, 2695–2699.
4 S. Zhang, Z. Wang, Z. Kong, Y. Wang, X. Zhang, B. Sun, H. Zhang, Q. Kan, Z. He, C. Luo and J. Sun, *Theranostics*, 2021, **11**, 6019–6032.
5 S. Onoue, S. Yamada and H. K. Chan, *Int. J. Nanomed.*, 2014, **9**, 1025–1037.
6 J. Rautio, H. Kumpulainen, T. Heimbach, R. Oliyai, D. Oh, T. Jarvinen and J. Savolainen, *Nat. Rev. Drug Discovery*, 2008, **7**, 255–270.
7 J. Nicolas, S. Mura, D. Brambilla, N. Mackiewicz and P. Couvreur, *Chem. Soc. Rev.*, 2013, **42**, 1147–1235.
8 M. Huo, L. Wang, Y. Chen and J. Shi, *Nat. Commun.*, 2017, **8**, 357.
9 S. V. Rana, *J. Trace Elem. Med. Biol.*, 2008, **22**, 262–284.
10 F. Lang and E. K. Hoffmann, *Compr. Physiol.*, 2012, **2**, 2037–2061.
11 M. Zhang, R. X. Song, Y. Y. Liu, Z. G. Yi, X. F. Meng, J. W. Zhang, Z. M. Tang, Z. W. Yao, Y. Liu, X. G. Liu and W. B. Bu, *Chem*, 2019, **5**, 2171–2182.
12 C. Zhang, W. B. Bu, D. L. Ni, S. J. Zhang, Q. Li, Z. W. Yao, J. W. Zhang, H. L. Yao, Z. Wang and J. L. Shi, *Angew. Chem., Int. Ed.*, 2016, **55**, 2101–2106.
13 A. M. Spokoyny, D. Kim, A. Sumrein and C. A. Mirkin, *Chem. Soc. Rev.*, 2009, **38**, 1218–1227.
14 W. Sang, Z. Zhang, G. H. Wang, L. S. Xie, J. Li, W. X. Li, H. Tian and Y. L. Dai, *Adv. Funct. Mater.*, 2022, **32**, 2113168.
15 S. Xu, J. Liu, D. Li, L. M. Wang, J. Guo, C. C. Wang and C. Y. Chen, *Biomaterials*, 2014, **35**, 1676–1685.
16 S. Zhang, S. Zhang, S. Y. Luo and D. C. Wu, *Coord. Chem. Rev.*, 2021, **445**, 214059.
17 K. Li, C. Lin, M. Li, K. Xu, Y. He, Y. Mao, L. Lu, W. Geng, X. Li, Z. Luo and K. Cai, *ACS Nano*, 2022, **16**, 2381–2398.
18 Y. Qin, F. Tong, W. Zhang, Y. Zhou, S. Q. He, R. Xie, T. Lei, Y. S. Wang, S. J. Peng, Z. F. Li, J. Leong, H. L. Gao and L. G. Lu, *Adv. Funct. Mater.*, 2021, **31**, 2104645.
19 B. Yu, B. S. Choi, W. G. Li and D. H. Kim, *Nat. Commun.*, 2020, **11**, 1–9.
20 Y. Xu, Y. Guo, C. Zhang, M. Zhan, L. Jia, S. Song, C. Jiang, M. Shen and X. Shi, *ACS Nano*, 2022, **16**, 984–996.
21 X. L. Ding, M. D. Liu, Q. Cheng, W. H. Guo, M. T. Niu, Q. X. Huang, X. Zeng and X. Z. Zhang, *Biomaterials*, 2022, **281**, 121369.
22 D. Zhao, W. Tao, S. Li, Y. Chen, Y. Sun, Z. He, B. Sun and J. Sun, *Sci. Adv.*, 2021, **7**, 0880.
23 L. Zhang, X. Gao, L. Yang, P. Yu and L. Mao, *ACS Appl. Mater. Interfaces*, 2013, **5**, 8120–8124.
24 H. Ejima, J. J. Richardson, K. Liang, J. P. Best, M. P. van Koeverden, G. K. Such, J. Cui and F. Caruso, *Science*, 2013, **341**, 154–157.
25 V. Kozlovskaya, O. Zavgorodnya, Y. Chen, K. Ellis, H. M. Tse, W. Cui, J. A. Thompson and E. Kharlampieva, *Adv. Funct. Mater.*, 2012, **22**, 3389–3398.
26 J. Chen, S. Ratnayaka, A. Alford, V. Kozlovskaya, F. Liu, B. Xue, K. Hoyt and E. Kharlampieva, *ACS Nano*, 2017, **11**, 3135–3146.
27 P. X. Wang, S. L. Liu, M. X. Hu, H. W. Zhang, D. M. Duan, J. Y. He, J. J. Hong, R. T. Lv, H. S. Choi, X. Y. Yan and M. M. Liang, *Adv. Funct. Mater.*, 2020, **30**, 2000647.
28 Y. Xiong, C. Xiao, Z. Li and X. Yang, *Chem. Soc. Rev.*, 2021, **50**, 6013–6041.
29 E. Kim, Y. Jeen, H. Cho, B. Keum, Y. Kim, H. Lee, H. Chun, C. Kim and H. Ryu, *J. Clin. Oncol.*, 2011, **29**, 463.
30 L. Galluzzi, A. Lopez-Soto, S. Kumar and G. Kroemer, *Immunity*, 2016, **44**, 221–231.
31 Y. Jiang, W. Meng, L. Wu, K. Shao, L. Wang, M. Ding, J. Shi and X. Kong, *Adv. Healthcare Mater.*, 2021, **10**, 2100789.
32 W. Bao, M. Liu, J. Meng, S. Liu, S. Wang, R. Jia, Y. Wang, G. Ma, W. Wei and Z. Tian, *Nat. Commun.*, 2021, **12**, 6399.